
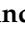



Article

In Vivo PET Imaging of Monocytes Labeled with [⁸⁹Zr]Zr-PLGA-NH₂ Nanoparticles in Tumor and *Staphylococcus aureus* Infection Models

Massis Krekorian ^{1,2,*}, Kimberley R. G. Cortenbach ¹, Milou Boswinkel ², Annemarie Kip ², Gerben M. Franssen ², Andor Veltien ², Tom W. J. Scheenen ², René Raavé ², Nicolaas Koen van Riessen ^{1,3}, Mangala Srinivas ^{1,3}, Ingrid Jolanda M. de Vries ¹, Carl G. Figdor ¹, Erik H. J. G. Aarntzen ² and Sandra Heskamp ²

- ¹ Department of Tumor Immunology, Radboud Institute for Molecular Life Sciences, Radboud University Medical Center, Geert Grooteplein 28, 6525 GA Nijmegen, The Netherlands; kim.cortenbach@radboudumc.nl (K.R.G.C.); Koen.vanRiessen@radboudumc.nl (N.K.v.R.); mangala.srinivas@wur.nl (M.S.); Jolanda.deVries@radboudumc.nl (I.J.M.d.V.); Carl.Figdor@radboudumc.nl (C.G.F.)
- ² Department of Medical Imaging, Radboud University Medical Center, Geert Grooteplein Zuid 10, 6525 GA Nijmegen, The Netherlands; Milou.Boswinkel@radboudumc.nl (M.B.); akip@cityryll.com (A.K.); Gerben.Franssen@radboudumc.nl (G.M.F.); Andor.Veltien@radboudumc.nl (A.V.); Tom.Scheenen@radboudumc.nl (T.W.J.S.); Rene.Raave@radboudumc.nl (R.R.); Erik.Aarntzen@radboudumc.nl (E.H.J.G.A.); Sandra.Heskamp@radboudumc.nl (S.H.)
- ³ Cerna Imaging BV, Tweede Kostverlorenkade 11H, 1052 RK Amsterdam, The Netherlands
- * Correspondence: massis.krekorian@radboudumc.nl



Citation: Krekorian, M.; Cortenbach, K.R.G.; Boswinkel, M.; Kip, A.; Franssen, G.M.; Veltien, A.; Scheenen, T.W.J.; Raavé, R.; van Riessen, N.K.; Srinivas, M.; et al. In Vivo PET Imaging of Monocytes Labeled with [⁸⁹Zr]Zr-PLGA-NH₂ Nanoparticles in Tumor and *Staphylococcus aureus* Infection Models. *Cancers* **2021**, *13*, 5069. <https://doi.org/10.3390/cancers13205069>

Academic Editor: Stefaan Willy van Gool

Received: 30 August 2021
Accepted: 4 October 2021
Published: 10 October 2021

Publisher's Note: MDPI stays neutral with regard to jurisdictional claims in published maps and institutional affiliations.



Copyright: © 2021 by the authors. Licensee MDPI, Basel, Switzerland. This article is an open access article distributed under the terms and conditions of the Creative Commons Attribution (CC BY) license (<https://creativecommons.org/licenses/by/4.0/>).

Simple Summary: Immune cells are increasingly used for therapy in cancer and other diseases. To better understand immune-cell kinetics, cell-tracking with highly sensitive imaging modalities is required. The aim of this study was to develop a new strategy for the in vivo tracking of a small number of cells, using positron emission tomography (PET). We labeled poly(lactic-co-glycolic acid) nanoparticles containing a primary endcap (PLGA-NH₂) with the radionuclide zirconium-89. The nanoparticles were characterized for size, polydispersity index, zeta potential and radiolabel retention. Subsequently, they were used for the ex vivo radiolabeling of a monocyte cell line (THP-1). We demonstrated that these radiolabeled monocyte cells can be traced in vivo in mouse tumor and infection models.

Abstract: The exponential growth of research on cell-based therapy is in major need of reliable and sensitive tracking of a small number of therapeutic cells to improve our understanding of the in vivo cell-targeting properties. ¹¹¹In-labeled poly(lactic-co-glycolic acid) with a primary amine endcap nanoparticles (¹¹¹In-PLGA-NH₂ NPs) were previously used for cell labeling and in vivo tracking, using SPECT/CT imaging. However, to detect a low number of cells, a higher sensitivity of PET is preferred. Therefore, we developed ⁸⁹Zr-labeled NPs for ex vivo cell labeling and in vivo cell tracking, using PET/MRI. We intrinsically and efficiently labeled PLGA-NH₂ NPs with [⁸⁹Zr]ZrCl₄. In vitro, [⁸⁹Zr]Zr-PLGA-NH₂ NPs retained the radionuclide over a period of 2 weeks in PBS and human serum. THP-1 (human monocyte cell line) cells could be labeled with the NPs and retained the radionuclide over a period of 2 days, with no negative effect on cell viability (specific activity 279 ± 10 kBq/10⁶ cells). PET/MRI imaging could detect low numbers of [⁸⁹Zr]Zr-THP-1 cells (10,000 and 100,000 cells) injected subcutaneously in Matrigel. Last, in vivo tracking of the [⁸⁹Zr]Zr-THP-1 cells upon intravenous injection showed specific accumulation in local intramuscular *Staphylococcus aureus* infection and infiltration into MDA-MB-231 tumors. In conclusion, we showed that [⁸⁹Zr]Zr-PLGA-NH₂ NPs can be used for immune-cell labeling and subsequent in vivo tracking of a small number of cells in different disease models.

Keywords: PLGA-NH₂ nanoparticles; PET/MRI imaging; zirconium-89 labeling; in vivo tracking; primary amine; cell labeling

1. Introduction

Cell-based therapy is maturing into clinical practice and holds great promise for treating cancer, as well as immune-related diseases. In vivo cell tracking is desired to better understand the complex cell targeting mechanism and cell–cell interactions. For example, such tools could guide the development of treatment strategies to increase tumor-targeting and minimize off-target accumulation and associated toxicity [1–4]. The effector immune-cell populations involved in these therapeutic interventions reach peripheral tissues in relatively small numbers, in the order of a few thousand [5–9]. Therefore, stable labeling of immune cells and a highly sensitive imaging system with adequate tissue penetration depth for whole-body imaging are required.

For direct cell labeling, specific cell (sub)types are isolated from patients and labeled ex vivo. For example, T cells can be labeled with highly derivatized crosslinked iron oxide nanoparticles (NPs) and detected with magnetic resonance imaging (MRI) [10]. Although magnetic particle imaging (MPI) is a highly sensitive technique (detection of ~200 cells and a resolution of ~1 mm), there are currently no clinically available scanners [11–14]. In contrast, positron emission tomography (PET) is commonly applied in clinical practice for diagnosis, staging and response monitoring in cancer and other diseases. PET tracking of radiolabeled cells is traditionally performed with lipophilic compounds, including oxine and hexamethylpropyleneamine oxime (HMPAO), that passively diffuse across the cell membrane [15]. In clinical settings, [¹¹¹In]In-oxine and [^{99m}Tc]Tc-HMPAO are used in combination with single-photon emission computed tomography (SPECT) imaging [16,17]. Although this labeling strategy is fast and results in a good labeling efficiency, it has several drawbacks. In particular, it has been shown that cells labeled with [¹¹¹In]In-oxine release the radionuclide up to 50% within 48 h [18], and the oxine carrier appears to be chemotoxic [19]. Furthermore, clinical SPECT systems have a low sensitivity and resolution, which hamper the tracking of low numbers of cells distributed over a large volume. In contrast, PET has a higher resolution, sensitivity and more accurate quantification compared to SPECT. New developments in PET technology hold promise for even higher sensitivity compared to current PET scanners [20]. Therefore, PET-based in vivo cell tracking is preferred over SPECT in the clinical setting. In this study, we introduced the radiometal zirconium-89 (⁸⁹Zr) as a positron emitter, with an ideal half-life (78.41 h) for cell tracking.

More recently, [⁸⁹Zr]Zr-oxine has been introduced for PET-based cell tracking [21,22], but it experiences similar limitations to those observed with [¹¹¹In]In-oxine [23,24]. A multitude of ⁸⁹Zr-labeled NPs for different applications have been reported previously [25–27]. For example, chitosan NPs have also been used for ⁸⁹Zr-labeling of leukocyte cells [28]. The intrinsic labeling of the chitosan NPs was suggested to be possible via the interaction of the ⁸⁹Zr with the OH and NH₂ groups. High cell-labeling efficiency was achieved with up to 73% after 24 h. However, the ⁸⁹Zr-release from the cells was also rapid, with up to 79% after 24 h. No specific activity per number of cells was reported, making it difficult to compare to other studies. In another study, in vivo tumor-associated macrophages were targeted and imaged by using ⁸⁹Zr-desferrioxamine-NCS (DFO) conjugated dextran NPs in colon carcinoma (CT26) tumor xenograft mice [25]. Here, also some release was detected in the bones with PET images. Radiolabel release by ex vivo labeled cells is a hurdle for sensitive and specific in vivo cell tracking, as free radionuclides accumulate in off-target tissue and could lead to higher background signal and potential misinterpretation of images, while also exposing tissue to unnecessary radiation dose [29,30].

In our previous work, we have shown that poly(lactic-co-glycolic acid) NPs with amine groups (PLGA-NH₂ NPs) can be used to radiolabel cells and demonstrates improved radiolabel retention compared with the oxine labeling method [31]. Here, we report the

intrinsic labeling capacity of these NPs with [^{89}Zr]ZrCl₄ under various conditions. In vitro, immortalized human monocytes (THP-1) were labeled with [^{89}Zr]Zr-PLGA-NH₂ NPs and the retention of ^{89}Zr in the cell was studied over time. Finally, we show that it is feasible to image ex vivo labeled THP-1 cells with PET in mice with *Staphylococcus aureus* (*S. aureus*) inflamed muscles or human breast adenocarcinoma MDA-MB-231 tumors.

2. Materials and Methods

2.1. Synthesis of Nanoparticles

The same preparation protocol was used as described before [31]. Briefly, 100 mg of poly(lactic-co-glycolic acid) diamine endcap copolymer (PLGA-NH₂, Mn = 5000, Sigma-Aldrich, Merck, Saint Louis, MO, USA), 200 μL of poly(propylene glycol) (PPO, 50 mg/mL stock, Sigma-Aldrich, average Mn 2700) and 900 μL perfluoro-15-crown-5-ether (PFCE, Exflur Inc., Round Rock, TX, USA) were dissolved in 3 mL dichloromethane (DCM, Merck, Darmstadt, Germany). Simultaneously, 500 mg of poly(vinyl alcohol) (PVA, Mw 9000–10,000 Da, 80% hydrolyzed, Sigma-Aldrich) was dissolved in 25 g of MilliQ (18.2 M Ω cm, Merck, Kenilworth, NJ, USA). The organic phase was mixed and rapidly added to the PVA solution during sonication for 3 min, at 40% amplitude, with a probe sonicator (Sonifier 250, microtip 6.4 mm, Branson Sonic Power, Saint Louis, MO, USA). The organic phase was left to evaporate overnight, at 4 $^{\circ}\text{C}$, while stirring. After washing the NPs four times with MilliQ and snap-freezing in liquid nitrogen, the samples were lyophilized for 48 h and stored at -20°C until needed.

2.2. Characterization of Nanoparticles

PLGA-NH₂ NPs were analyzed for size, polydispersity index (PDI) and zeta potential, in the same way as in our previous study [31]. The NPs were dissolved at 0.1 mg/mL in MilliQ, and both size and PDI were measured by using a NANO-flex (Microtrac, Inc., Duesseldorf, Germany), and the data were analyzed by using Microtrac software (Microtrac FLEX 11.1.0.2, Duesseldorf, Germany). The zeta potential was measured by using Zetasizer Nano ZS (Malvern Instruments, Worcestershire, United Kingdom), where similar NP concentrations were dissolved in NaCl (5 mM, pH 7.4). Encapsulation efficiency of PFCE was measured by using a nuclear magnetic resonance (NMR, Bruker Avance III 400 MHz, Bruker BioSpin, Ettlingen, Germany) spectrometer coupled with a Broad Band Fluorine Observation (BBFO) probe. NPs, ~5 mg, were dissolved in 500 μL deuterium oxide (D₂O) containing 100 μL 1 volume% trifluoroacetic acid (TFA) in D₂O. For quantification, the interscan relaxation delay (D1) was set at 5 times the relaxation time (T1) of TFA, at 20 s. The data were evaluated with Mestrenova 10.0.2 (Mestrelab Research, Escandido, CA, USA).

2.3. Characterization of Nanoparticles Stability in Human Serum and PBS over Time

PLGA-NH₂ and Zr-PLGA-NH₂ NPs' size and PDI were measured in 100% human serum (human male AB plasma, Sigma-Aldrich, USA) and PBS at 0, 1, 2, 4, 6, 24, 48, 72, 168 and 336 h. First, the NPs were labeled with non-radioactive zirconium (932 μg zirconium/mg NP in 0.05 M HCl, pH 1.1–1.4, MO, USA) in metal-free 0.5 M ammonium acetate (NH₄Ac, pH 5.5), which is similar to ^{89}Zr -labeling (see Zirconium-89 labeling of PLGA and PLGA-NH₂ NPs). Second, both PLGA and Zr-PLGA-NH₂ NPs were dissolved at a concentration of 10 mg/mL in PBS or 100% human serum. The samples were incubated at 37 $^{\circ}\text{C}$, in a thermomixer, for the indicated timepoints. Last, 10 μL of NP solution was transferred to 990 μL MilliQ (0.1 mg/mL), and both size and PDI were measured as explained above.

2.4. [^{89}Zr]ZrCl₄ Preparation from ^{89}Zr -Oxalate

In order to obtain [^{89}Zr]ZrCl₄, we removed oxalate by using a Sep-Pak Light Accell Plus QMA Cartridge (Waters, Dublin, Ireland). The Sep-Pak was activated with 10 mL acetonitrile and then washed with 10 mL 0.9% NaCl, 10 mL 1 M HCl and 10 mL water.

[⁸⁹Zr]Zr-oxalate (Cyclotron VU, Amsterdam, The Netherlands) was added, and the cartridge was washed with 50 mL water. Finally, the ⁸⁹Zr-label was eluted with 1 mL HCl (0.1 M) in 100 µL aliquots.

2.5. Intrinsic ⁸⁹Zr-Labeling of PLGA and PLGA-NH₂ NPs

This experiment was performed in the same manner as described in our previous study [31]. For intrinsic labeling, 1 mg NPs were dissolved in 0.5 M NH₄Ac and incubated with 1–5 MBq [⁸⁹Zr]ZrCl₄, at 37 °C, for 30 min. After washing the NPs 3 times with PBS, the labeling efficiency and radiochemical purity were determined with instant Thin-Layer Chromatography (iTLC). Labeling efficiency was calculated as the fraction of radioactivity at the origin to the total amount of radioactivity. Unless otherwise stated, the NPs were washed until a radiochemical purity of >95% was obtained. All radioactive labeling was performed in 0.5 M NH₄Ac, pH 5.5, unless stated otherwise.

2.6. ⁸⁹Zr-Retention of PLGA-NH₂ NPs in PBS and Human Serum

[⁸⁹Zr]Zr-PLGA-NH₂ NPs (1–5 MBq/mg, 10 mg/mL) were incubated in 100% human serum and PBS, at 37 °C, for 2 weeks. The ⁸⁹Zr-retention was measured at 0, 1, 2, 4, 6, 24, 48, 72 and 336 h after incubation with iTLC.

2.7. EDTA Challenge

[⁸⁹Zr]Zr-PLGA-NH₂ NPs (3 MBq/mg, 10 mg/mL) were challenged with 0.1, 1, 10 and 50 mM EDTA (corresponds to approximately 0.1, 1, 10 and 50 equivalents more EDTA to NP) in PBS at 37 °C for 2 weeks. At 0, 1, 2, 4, 6, 24, 48, 72, 168 and 336 h, samples of 1 µL were analyzed with iTLC.

2.8. Cell Culture

The immortalized human monocyte cell line THP-1 (ATCC[®] TIB-202[™], VA, Gaithersburg, MD, USA) was used for cell labeling (passage of <20). The cells were maintained in culture as described previously [31].

The human adenocarcinoma cell line (MDA-MB-231, passage 46, ATCC[®] HTB-26[™], Gaithersburg, MD, USA) was cultured under the same conditions.

2.9. [⁸⁹Zr]Zr-PLGA-NH₂ NP Labeling of THP-1 Cell Line and Retention of Radiolabel over Time

THP-1 cells were incubated with [⁸⁹Zr]Zr-PLGA-NH₂ NPs, at a concentration of 7.5 ± 0.3 MBq/1 mg NP/10⁶ cells, at 37 °C, for 2 h. As a control, we treated the THP-1 cells in the same manner, without the addition of [⁸⁹Zr]Zr-PLGA-NH₂ NPs, but with PBS. Subsequently, cells were washed to remove NPs which were not taken up by the cells. After labeling and washing, cells were incubated at culture conditions for 1, 2, 4, 6, 24 and 48 h. At every timepoint, the cells were first measured for radioactivity for 1 min with a γ-counter (wizard 2480 Automatic Gamma Counter, PerkinElmer, Downers Grove, IL, USA). The cells were then centrifuged at 300× g for 5 min, the supernatant was removed and the cells were resuspended in fresh PBS before another radioactivity measurement. The percentage retained radioactivity in the cells was calculated by dividing the activity measured after removal of supernatant by total amount of radioactivity before centrifugation, multiplied by 100.

2.10. Cell Counting

Cell numbers after an experiment were counted with Luna-II Automated Cell Counter (Logos Biosystems, Inc., Anyang, South Korea). The mixture of cells with trypan blue (1:1) was transferred to a counting cassette (Logos Biosystems, Inc., Korea) before automated counting. Living cells were used for calculating the specific activity per number of cells by dividing the total activity associated with the pellet with the number of living cells times hundred.

2.11. CellTiter-Glo Assay

For ATP content measurement, 80,000 cells were diluted with PBS to a volume of 350 μ L and mixed with 350 μ L of premixed substrate and buffer CellTiter-Glo (Promega, Madison, WI, USA). After a short vortex, the samples were incubated for 10 min, at room temperature (RT). From each sample, 200 μ L in triplicate was transferred to a 96-wells plate (black flat bottom), and luminescence was measured by using a Tecan Infinite M200 PRO and software Tecan i-control (attenuation automatic, integration time 1000 millisecond, settle time 0 millisecond, Tecan, Grödigg, Austria). Controls were set to 100%, and sample results were compared to this.

2.12. Animal Experiments

For animal experiments, the guidelines set by the Nijmegen and European Animal Experiments Committee (CCD application 2018-0011 and 2020-0007) were followed. The animals were housed in groups in individually ventilated Blue line cages. To determine [^{89}Zr]Zr-PLGA-NH₂ NPs biodistribution and blood clearance, 6 female C57BL/6J mice (Janvier Labs) were used (age 6–8 weeks, weight 18.4 ± 1.2 g). For PET and MRI studies with [^{89}Zr]Zr-PLGA-NH₂ NPs labeled THP-1 cells in Matrigel, 12 female BALB/cAnNRj-Foxn1nu/Foxn1nu mice (Janvier Labs) were used (age 6–8 weeks, weight 20.0 ± 0.9 g). In vivo tracking of [^{89}Zr]Zr-THP-1 cells in *S. aureus* and MDA-MB-231 tumor models were performed in 11 female BALB/cAnN.Cg-Foxn1nu/Crl mice (Charles River) (age 6–8 weeks, weight 16.5 ± 2.3 g). The mice were allowed to acclimate for 1 week before the start of the experiments. Upon arrival, the mice were randomly identified with tattoos by biotechnicians who were blinded to the experimental setup.

2.13. [^{89}Zr]Zr-PLGA-NH₂ NPs Biodistribution and Blood Clearance in C57BL/6J Mice

At day 0, all mice were i.v. injected via the tail vein with 200 μ L PBS containing 1.81 ± 0.61 MBq/5 mg [^{89}Zr]Zr-PLGA-NH₂ NPs (the particles were washed until <5% release of free ^{89}Zr was measured compared to previous washing step). For blood kinetics, blood samples were collected via saphenous vein or heart puncture (when sacrificed), at 30 min (3 mice), 1 h (6 mice), 2 h (3 mice), 4 h (6 mice), 24 h (6 mice), day 2 (6 mice), day 3 (6 mice), day 7 (3 mice) and day 14 (3 mice). For ex vivo biodistribution, organs (spleen, liver, kidney, heart, lungs, pancreas, bladder, duodenum, ileum, colon, brain, muscle, lymph nodes (LN, inguinal), femur, bone marrow, thymus, brown fat, stomach, salivary glands and knees) were harvested after euthanizing the mice with CO₂/O₂ asphyxiation at day 3 (3 mice) and day 14 (3 mice). Radioactivity of the blood and organs was measured for 1 min with a γ -counter. Tissue and blood were measured for % injected dose per gram (%ID/g) with simultaneous measurements of aliquots from injected fluid. GraphPad Prism (GraphPad Software Inc., San Diego, CA, USA) was used for calculating the blood half-life ($t_{1/2}$) with nonlinear regression with one-phase decay, as computed by using the formula $\ln(2)/K$, with K as a rate constant, expressed in reciprocal of the x-axis time units.

For in vivo PET/MRI imaging, mice were anesthetized by using isoflurane in oxygen (33% oxygen + 67% air) before imaging. Isoflurane (5%) was used for induction and maintained at 1–2% during scanning. Mice were imaged at 1 h (3 mice), 4 h (3 mice), 24 h (3 mice), day 3 (3 mice), day 7 (3 mice) and day 14 (3 mice) with PET (Siemens Preclinical Solution) and followed immediately by MRI (Bruker ClinScan 70/30 7T, Bruker BioSpin, Ettlingen, Germany). During scanning, the temperature of the mice was maintained at 37 °C, using a heating bed. For reconstruction of PET scans (30–60 min), Inveon Acquisition Workspace software (version 1.5, Siemens Preclinical Solution, Erlangen, Germany) was used with the reconstruction algorithm OSEM3D/SO-MAP and the following settings: no scatter correction; using scale factor, 0; matrix, 256 \times 256; image zoom, 1; frames, all; OSEM Iterations, 2; MAP Iterations, 18; target resolution, 1.5 mm; voxel size, 0.4 \times 0.4 \times 0.8 mm.

Immediately following the PET scan, mice were transported by using the same imaging bed to the MRI scanner for anatomical imaging, where they were scanned for a duration of 32 min. A birdcage body coil (Bruker BioSpin, Ettlingen, Germany) with 86 mm inner

diameter was used for image acquisition. After a localizer scan, the following settings were used for the 3D gradient echo scans: acquisition time = 32 min; repetition time = 30 ms; echo time = 1.3 ms; flip angle = 15 degrees; field of view = $120 \times 56 \times 32$ mm; and matrix = $576 \times 270 \times 160$, resulting in an isotropic resolution of 0.20 mm^3 .

The PET/MRI images were merged, and Inveon Research Workplace software (version 4.1) was used to create maximum-intensity projections. For the overlay, a reference tube with ^{89}Zr in PBS was placed on the scan bed.

2.14. PET and MRI Imaging of [^{89}Zr]Zr-PLGA-NH₂ NPs Labeled THP-1 Cells in Matrigel

At day 0, 10,000 ($395 \pm 179 \text{ Bq}$, $n = 4$) or 100,000 ($3950 \pm 1790 \text{ Bq}$, $n = 4$) of [^{89}Zr]Zr-THP-1 cells suspended in PBS were mixed with Matrigel (2:1 (v/v) PBS:Matrigel, BD Matrigel Matrix Basement Membrane (20.20 MG/ML), BD Biosciences, Bedford, MA, USA) before 200 μL was s.c. injected in the flank lower part of the back and abdomen. In addition, a mixture of Matrigel (1:1) and $1.56 \pm 0.47 \mu\text{g}$ [^{89}Zr]Zr-PLGA-NH₂ NPs ($3400 \pm 2194 \text{ Bq}$, $n = 4$) in PBS was s.c. injected as a control. For blood kinetics, blood samples were collected via saphenous vein or heart puncture (after sacrifice) at 30 min (4 mice), 1 h (4 mice), 4 h (4 mice) and 24 h (6 mice). For ex vivo biodistribution, organs and Matrigel were harvested and measured as described previously.

For in vivo PET/MRI imaging, mice were imaged at 1 h (4 mice) and 24 h (4 mice) with PET and followed immediately by MRI (Bruker BioSpec 117/16 11.7T, Bruker BioSpin, Ettlingen, Germany). For PET, the same settings were used as previously described.

Immediately following the PET scan, mice were transported by using the same imaging bed to the MRI scanner for anatomical imaging, where they were scanned for a duration of 45 min. A birdcage body coil (Bruker BioSpin, Ettlingen, Germany) with 72 mm inner diameter was used for image acquisition. After a localizer scan, the following settings were used for the 3D gradient echo scans: acquisition time = 42 min; repetition time = 100 ms; echo time = 2.2 ms; flip angle = 30 degrees; field of view = $100 \times 40 \times 40$ mm; and matrix = $400 \times 160 \times 160$, resulting in an isotropic resolution of 0.25 mm^3 .

2.15. In Vivo Tracking of [^{89}Zr]Zr-THP-1 Cells in *S. aureus* and MDA-MB-231 Tumor Models

S. aureus was purchased from QM Diagnostics (1.05×10^9 Colony-Forming Units (CFU)/mL PBS). At day -2 , *S. aureus* was mixed (1:1) with freshly extracted blood from donor mice, and 50 μL of the mixture was injected intramuscular in the right hind leg of mice ($n = 5$). In addition, PBS was mixed (1:1) with donor blood, and 50 μL was injected in the contralateral hind leg muscle of the same mice. At day 0, [^{89}Zr]Zr-THP-1 cells (5.8×10^6 cell/mouse, $90.75 \pm 12.84 \text{ kBq/mouse}$) were injected i.v. via the tail vein.

For the tumor model, MDA-MB-231 cells (5×10^6 cells/mouse) were suspended in RPMI-1640 medium, mixed with Matrigel (1:1) and injected s.c. in the right hind back side at day -22 ($n = 5$, 200 $\mu\text{L/mouse}$). When tumors reached a size of approximately 0.1 cm^3 , [^{89}Zr]Zr-THP-1 cells were injected i.v. via the tail vein (5×10^6 cells/mouse, $164.80 \pm 12.99 \text{ kBq/mouse}$).

For PET/MRI imaging and processing of images, the same settings were used as in PET and MRI imaging of [^{89}Zr]Zr-PLGA-NH₂ NPs labeled THP-1 cells in Matrigel.

2.16. Statistical Analysis

Statistical analysis was performed in GraphPad Prism software. A Gaussian distribution with a two-tailed unpaired Student's *t*-test was used to analyze differences in two groups. A *p*-value of <0.05 was considered statistically significant. When comparing three or more groups, a one-way ANOVA test with a Tukey test correction of multiple comparisons was performed. A two-way ANOVA test with a Sidak correction of multiple comparisons was used in the biodistribution experiments (Figure 2A), while a Tukey's correction was used to compare the groups in the Matrigel experiments (Figure 5A). All comparisons were based on a minimum of three replicates.

3. Results

3.1. Characterization of Particles

The PLGA-NH₂ particles, prepared as described previously [31], were labeled with non-radioactive zirconium (Zr) and characterized for diameter, polydispersity (PDI) and zeta potential (Table 1). The diameter increased slightly when the PLGA-NH₂ NPs were labeled with zirconium from 189 ± 1.9 nm to 196 ± 4.1 nm. The PDI remained the same while the zeta potential increased to a more neutral charge, from −2.3 ± 0.9 mV to −0.3 ± 0.4 mV. These results indicate that NP characteristics were altered by the Zr-labeling, with increased size and zeta potential.

Table 1. Characterization of PLGA-NH₂ and Zr-PLGA-NH₂ NPs: size ($n = 3$), PDI ($n = 3$) and zeta potential ($n = 3$).

Sample	Diameter (nm)	Polydispersity (PDI)	Zeta Potential (mV)
PLGA-NH ₂	189 ± 1.9	0.07	−2.3 ± 0.9
Zr-PLGA-NH ₂	196 ± 4.1	0.07	−0.3 ± 0.4

3.2. Stability of the PLGA-NH₂ and Zr-PLGA-NH₂ NPs in PBS and Human Serum

To assess whether the characteristics of the particles changed over time, we incubated the PLGA-NH₂ and Zr-PLGA-NH₂ NPs in PBS and 100% human serum at 37 °C for a period of 2 weeks. The diameter of the NPs remained stable (~200 nm) in PBS for 72 h and was increased (~300 nm) at 336 h (Figure S1A). Similarly, the PDI of both NPs remained stable (~0.08) for 72 h and was increased (~0.2) at 336 h. In human serum, the diameter of the NPs was increased (>200 nm) at 336 h (Figure S1B). The PDI of both samples showed similar fluctuations as observed for the diameter over time.

3.3. [⁸⁹Zr]ZrCl₄ Labeling of PLGA and PLGA-NH₂ NPs

PLGA and PLGA-NH₂ NPs were radiolabeled with [⁸⁹Zr]ZrCl₄, where a labeling efficiency of 7.1 ± 0.9% and 101.5 ± 1.1% for PLGA NPs and PLGA-NH₂ NPs ($p < 0.0001$, Figure 1A) was observed, respectively, showing efficient ⁸⁹Zr-labeling of PLGA-NH₂ NPs, without the need for additional chelator. To evaluate the effect of buffer on labeling efficiency, the PLGA-NH₂ NPs were labeled in 0.5 M HEPES, MES and NH₄Ac buffer at a pH of 5.5 (Figure 1B). Labeling efficiency was highest for the NH₄Ac buffer (76 ± 2%, $p < 0.0001$ compared to HEPES and MES buffers). We therefore continued to label PLGA-NH₂ NPs in NH₄Ac buffer. The retention of the ⁸⁹Zr by the NPs was measured in PBS and 100% human serum. In PBS and 100% human serum, the ⁸⁹Zr-retention was ~85 ± 15% after 336 h (Figure 1C). In addition, [⁸⁹Zr]Zr-PLGA-NH₂ NPs were challenged with EDTA at 37 °C, for 336 h. After an initial release of ⁸⁹Zr from the NPs during the first 6 h, a gradual and EDTA concentration-dependent release of ⁸⁹Zr was observed for up to 336 h (Figure 1D). From these results, we can conclude that ⁸⁹Zr was interacting with the PLGA-NH₂ NPs and retained by the NPs in PBS and human serum. However, the ⁸⁹Zr-label could be challenged by EDTA.

3.4. In Vivo Biodistribution of [⁸⁹Zr]Zr-PLGA-NH₂ NPs in C57BL/6 Mice

The in vivo biodistribution of [⁸⁹Zr]Zr-PLGA-NH₂ NPs upon intravenous (i.v.) injection was evaluated in C57BL/6 mice. The concentration of [⁸⁹Zr]Zr-PLGA-NH₂ NPs in blood decreased rapidly, and the calculated blood half-life ($t_{1/2}$) was 28 ± 6 min (Figure 2A and Table S1).

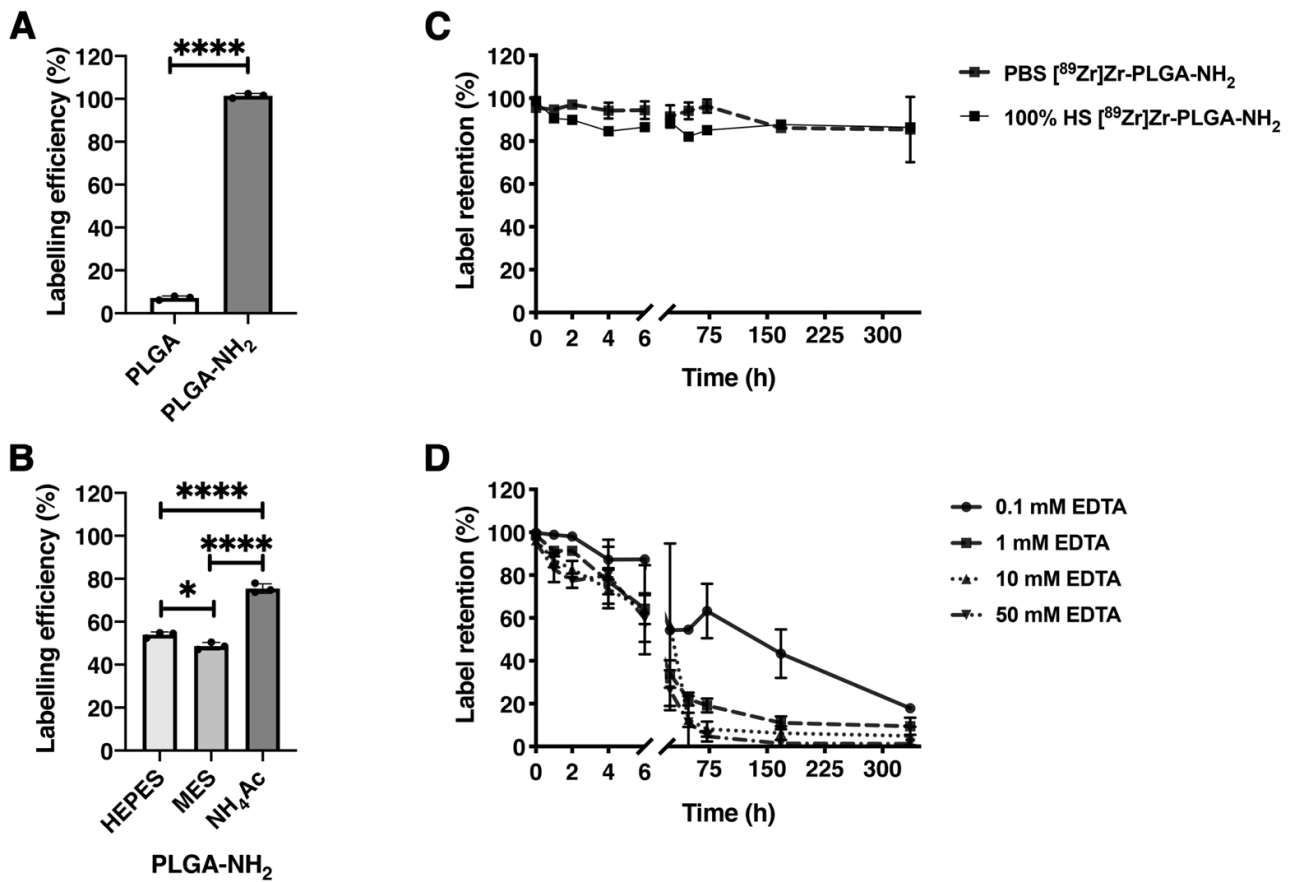


Figure 1. ⁸⁹Zr-labeling of NPs and label retention. (A) Labeling efficiency of PLGA and PLGA-NH₂ NPs with [⁸⁹Zr]ZrCl₄ (n = 3). (B) ⁸⁹Zr-labeling of PLGA-NH₂ NPs in 0.5 M and pH 5.5 HEPES, MES and NH₄Ac labeling buffers (n = 3). (C) ⁸⁹Zr-retention by PLGA-NH₂ NPs was examined in PBS and 100% human serum (100% HS) at 37 °C at 0, 1, 2, 4, 6, 24, 48, 72, 168 and 336 h (n = 3). (D) EDTA concentration range challenge was performed at 37 °C at 0, 1, 2, 4, 6, 24, 48, 72, 168 and 336 h (n = 3). * p = 0.0276, **** p < 0.0001.

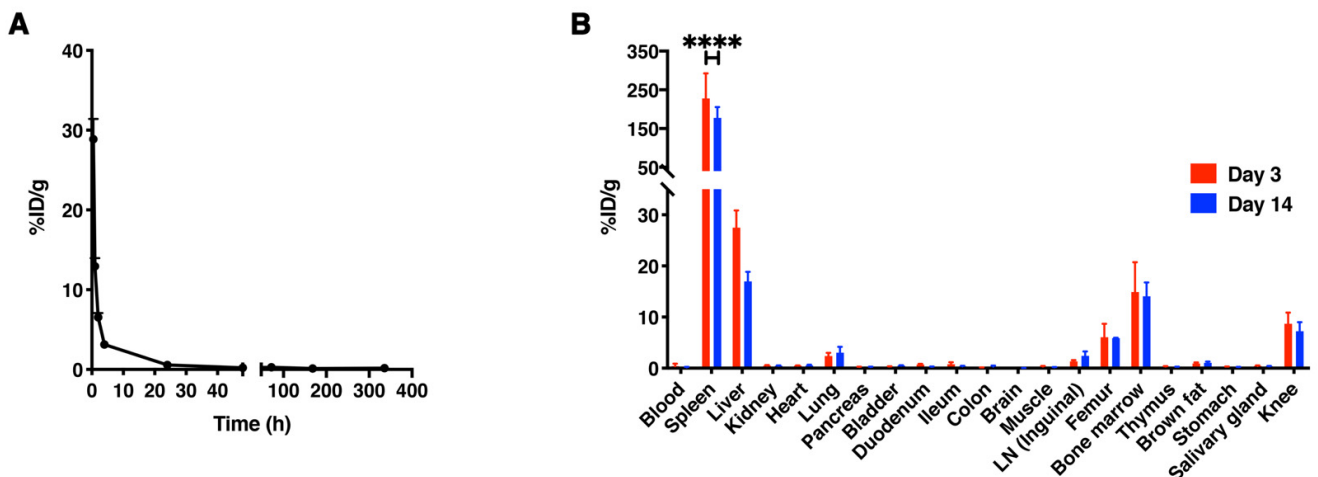


Figure 2. Blood clearance and biodistribution of [⁸⁹Zr]Zr-PLGA-NH₂ NPs. (A) [⁸⁹Zr]Zr-PLGA-NH₂ NPs clearance from blood after intravenously injection in C57BL/6 mice, measured at 0.5, 1, 2, 4, 6, 24, 48, 72, 168 and 336 h (n = 3–6). (B) Organ accumulation of the [⁸⁹Zr]Zr-PLGA-NH₂ NPs at day 3 and day 14 post-injection (n = 3 per group). Abbreviations: %ID/g, % injected dose per gram of organ; LN, lymph node. **** p < 0.0001.

Spleen, liver and bone marrow were the main organs for NP accumulation, as demonstrated by the result of the ex vivo measurements and PET/MRI scans (Figures 2B and 3 and Table S1). In addition, we also observed accumulation in femur ($5.9 \pm 0.1\%$ ID/g at day 14) and knees ($7.2 \pm 1.8\%$ ID/g at day 14). Taken together, these results show that the particles are cleared from the blood in the first 24 h after injection and that the spleen, liver and bone marrow are the main accumulation sites.

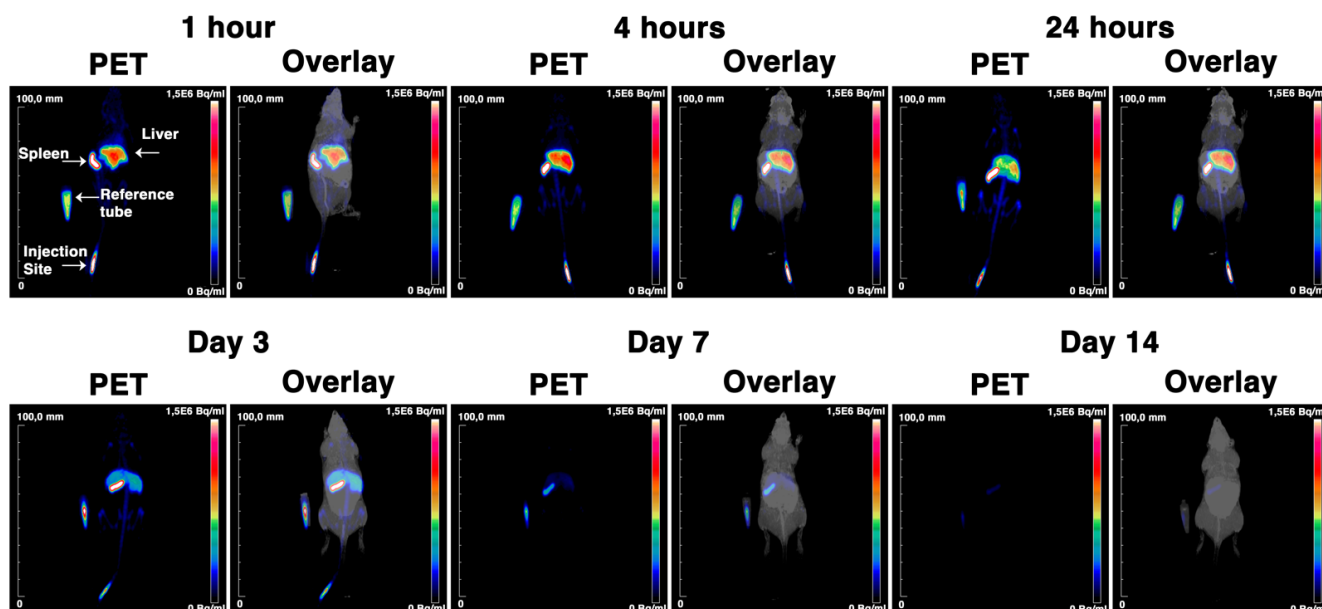


Figure 3. PET/MRI images of $[^{89}\text{Zr}]\text{Zr-PLGA-NH}_2$ NPs in C57BL/6 mice. C57BL/6J mice were intravenously injected with $[^{89}\text{Zr}]\text{Zr-PLGA-NH}_2$ NPs and imaged with PET/MRI at 1 h, 4 h, 24 h, 3 days, 7 days and 14 days post-injection. The reference tube contains 10% of the injected ^{89}Zr dose.

3.5. $[^{89}\text{Zr}]\text{Zr-PLGA-NH}_2$ NPs Labeling of THP-1 Cells and Retention over Time

THP-1 cells, immortalized human monocytes, were labeled with $[^{89}\text{Zr}]\text{Zr-PLGA-NH}_2$ NPs ($[^{89}\text{Zr}]\text{Zr-THP-1}$ cells), where a labeling efficiency of $4.03 \pm 0.16\%$ was observed, resulting in a specific activity of 279 ± 10 kBq/ 10^6 cells. The $[^{89}\text{Zr}]\text{Zr-THP-1}$ cells retained $79.6 \pm 5.9\%$ of the radiolabel at 48 h after incubation (Figure 4A). Cell counting showed that $76.4 \pm 15.2\%$ of $[^{89}\text{Zr}]\text{Zr-THP-1}$ cells remained alive over 48 h, while the ATP content, as measured with CellTiter-Glo assay in the cells, did not decrease ($119.7 \pm 9.4\%$ compared with control samples; Figure 4B,C). In summary, $[^{89}\text{Zr}]\text{Zr-PLGA-NH}_2$ NPs could stably label THP-1 cells, which remained viable over 48 h.

3.6. $[^{89}\text{Zr}]\text{Zr-THP-1}$ Cells for In Vivo PET/MRI Imaging

To determine PET sensitivity for the detection of low numbers of $[^{89}\text{Zr}]\text{Zr-THP-1}$ cells, three groups of mice were injected subcutaneously (s.c.) with Matrigel containing 10,000 $[^{89}\text{Zr}]\text{Zr-THP-1}$ cells, 100,000 $[^{89}\text{Zr}]\text{Zr-THP-1}$ cells or $[^{89}\text{Zr}]\text{Zr-PLGA-NH}_2$ NPs (Figure 5). All three Matrigel depositions were visible on the PET scans (Figure 6). From the biodistribution data, we can see that the blood and organ signals were low, indicating that the radioactive signal remains at the Matrigel for over 24 h (Figure 5 and Table S2).

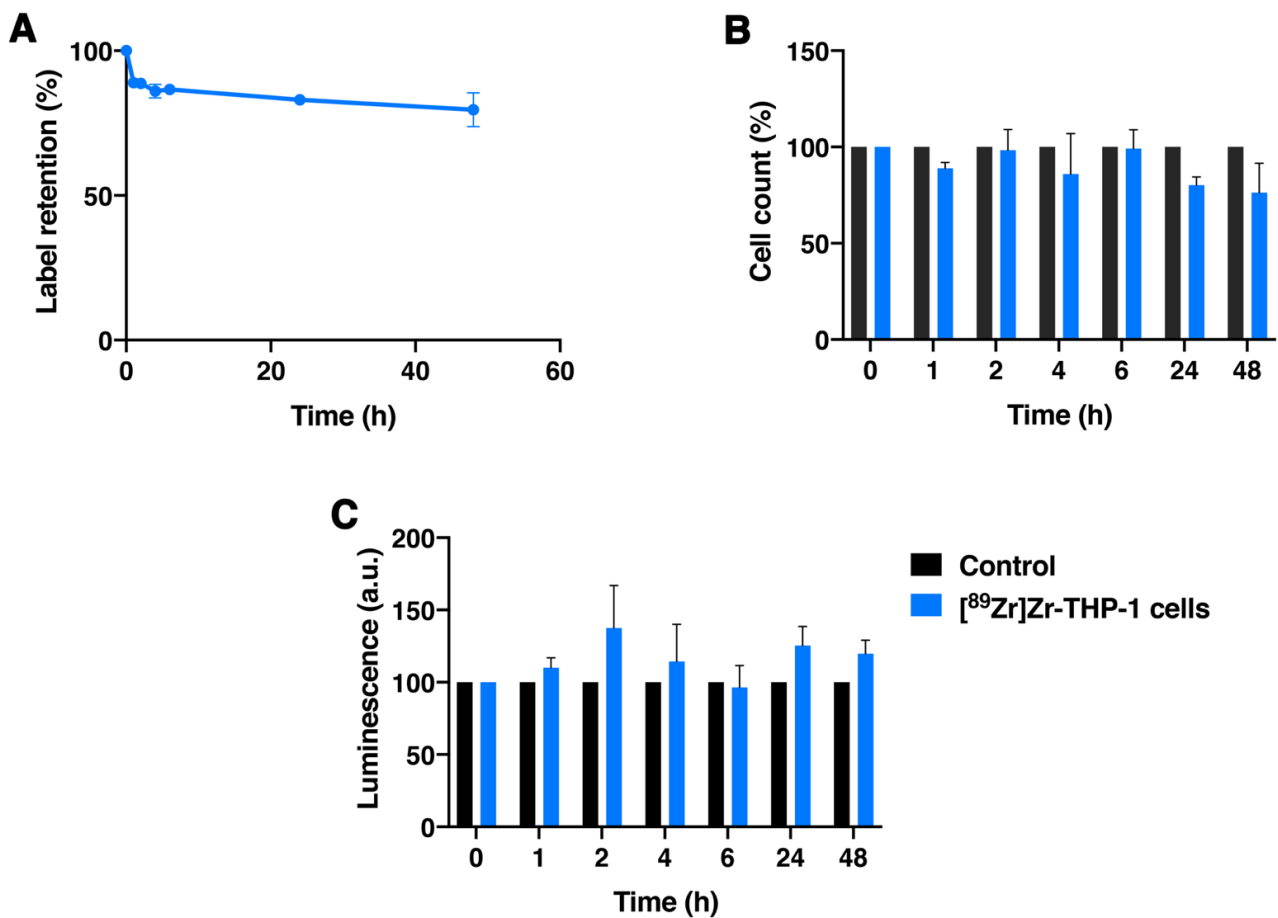


Figure 4. THP-1 labeling and retention of radionuclide over time. The ⁸⁹Zr-retention by THP-1 cells was measured for 1, 2, 4, 6, 24 and 48 h, at culture conditions; (A) the cells were measured for relative radioactivity after one spin; (B) viable cell numbers counted with trypan blue staining; and (C) the ATP content of cells as a measure with CellTiter-Glo for cell viability. In all experiments, controls are THP-1 cells which were treated in the same way as other conditions without [⁸⁹Zr]Zr-PLGA-NH₂ but with PBS. Moreover, the controls did not change in value over time and therefore were set to 100%, and the remaining samples were compared to the controls. The mean and standard deviation of at least three independent experimental datasets are shown.

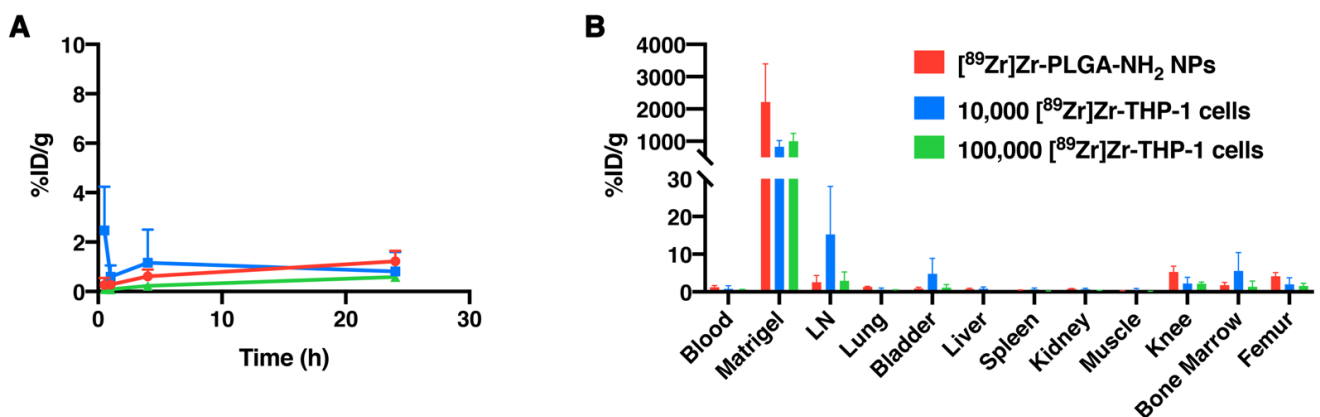


Figure 5. Blood values and biodistribution of [⁸⁹Zr]Zr-THP-1 cells in BALB/cAnNRj-Foxn1nu/Foxn1nu mice. (A) Blood values of [⁸⁹Zr]Zr-PLGA-NH₂ NPs (*n* = 4), 10,000 [⁸⁹Zr]Zr-THP-1 cells (*n* = 4) and 100,000 [⁸⁹Zr]Zr-THP-1 cells (*n* = 4) after subcutaneous injection in BALB/cAnNRj-Foxn1nu/Foxn1nu mice, measured at 0.5, 1, 4 and 24 h post-injection. (B) Matrigel and organ accumulation of the [⁸⁹Zr]Zr-PLGA-NH₂ NPs, 10,000 [⁸⁹Zr]Zr-THP-1 cells and 100,000 [⁸⁹Zr]Zr-THP-1 cells in the same mice. Abbreviations: %ID/g, % injected dose per gram of organ; LN, lymph node.

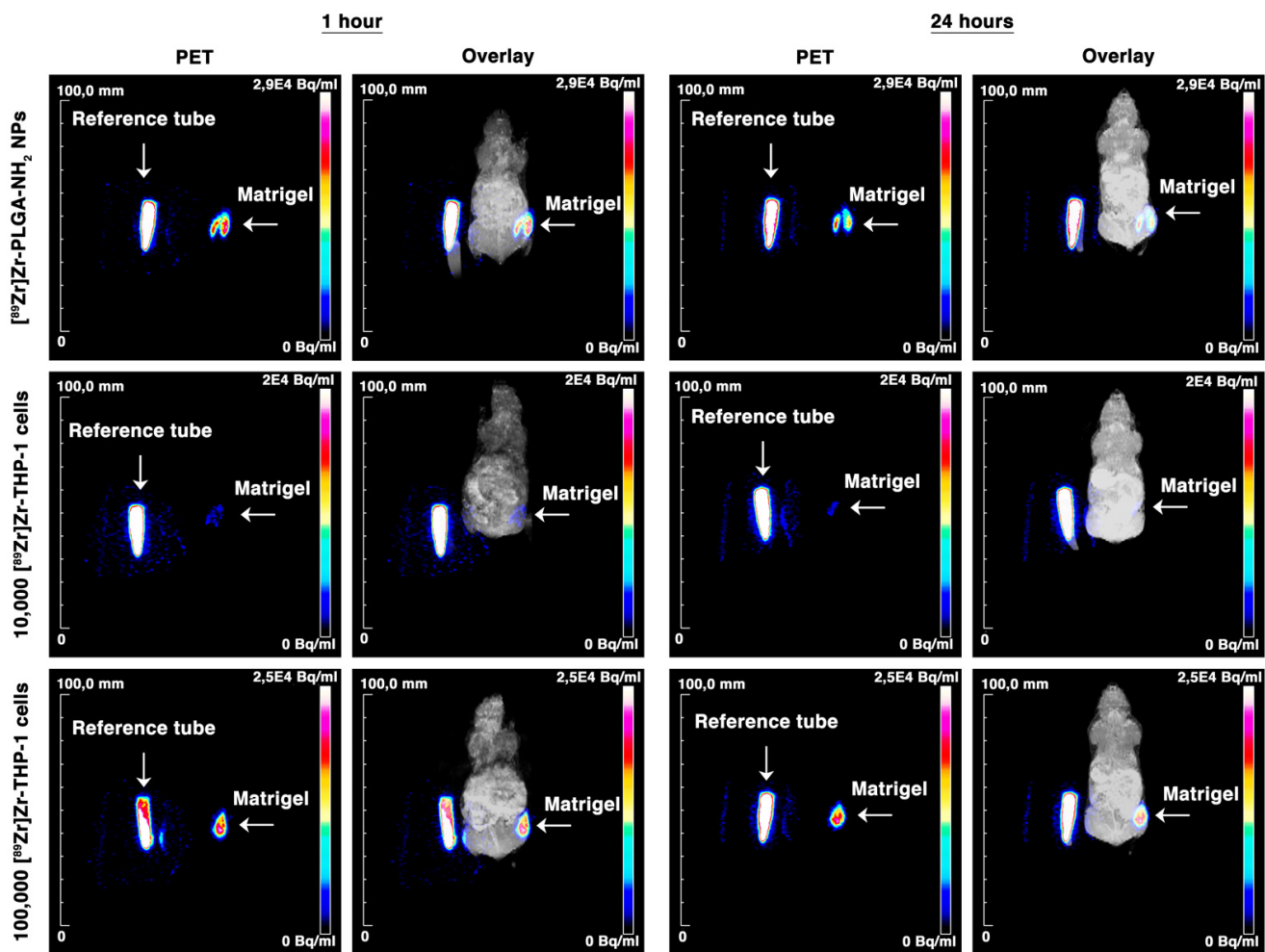


Figure 6. PET and MRI images of subcutaneous injected $[^{89}\text{Zr}]\text{Zr-THP-1}$ cells in BALB/cAnNRj-Foxn1nu/Foxn1nu mice. Mice were subcutaneously injected with Matrigel containing $[^{89}\text{Zr}]\text{Zr-PLGA-NH}_2$, 10,000 $[^{89}\text{Zr}]\text{Zr-THP-1}$ cells or 100,000 $[^{89}\text{Zr}]\text{Zr-THP-1}$ cells. PET and MRI scans were performed after 1 and 24 h. The reference tube contains 10% of the injected dose. Brightness (+100 points) and contrast (+70 points) were increased for better visualization, with Adobe Photoshop, in all the images.

3.7. In Vivo PET/MRI Tracking of $[^{89}\text{Zr}]\text{Zr-THP-1}$ Cells in Local *S. aureus* Infection and MDA-MB-231 Tumor Model

$[^{89}\text{Zr}]\text{Zr-THP-1}$ cells were tracked in vivo in a local intramuscular *S. aureus* infection and MDA-MB-231 tumor model. For the *S. aureus* model, i.v. injected $[^{89}\text{Zr}]\text{Zr-THP-1}$ cells were rapidly cleared from blood within 30 min. Ex vivo biodistribution study at 24 h showed that the organs with the highest uptake were spleen, liver, lung and bone marrow (Figure 7A,B and Table S3). Furthermore, $0.46 \pm 0.10\%$ of the total administered $[^{89}\text{Zr}]\text{Zr-THP-1}$ cells (corresponding to $26.89 \pm 5.79 \times 10^3$ cells) accumulated in the *S. aureus*-infected muscle, compared with $0.04 \pm 0.02\%$ ($2.14 \pm 0.89 \times 10^3$ cells) in the control muscle. A PET signal was detected as early as 4 h post-injection in the *S. aureus*-infected muscle, which increased at 24 h post-injection (Figure 8 and Videos S1 and S2).

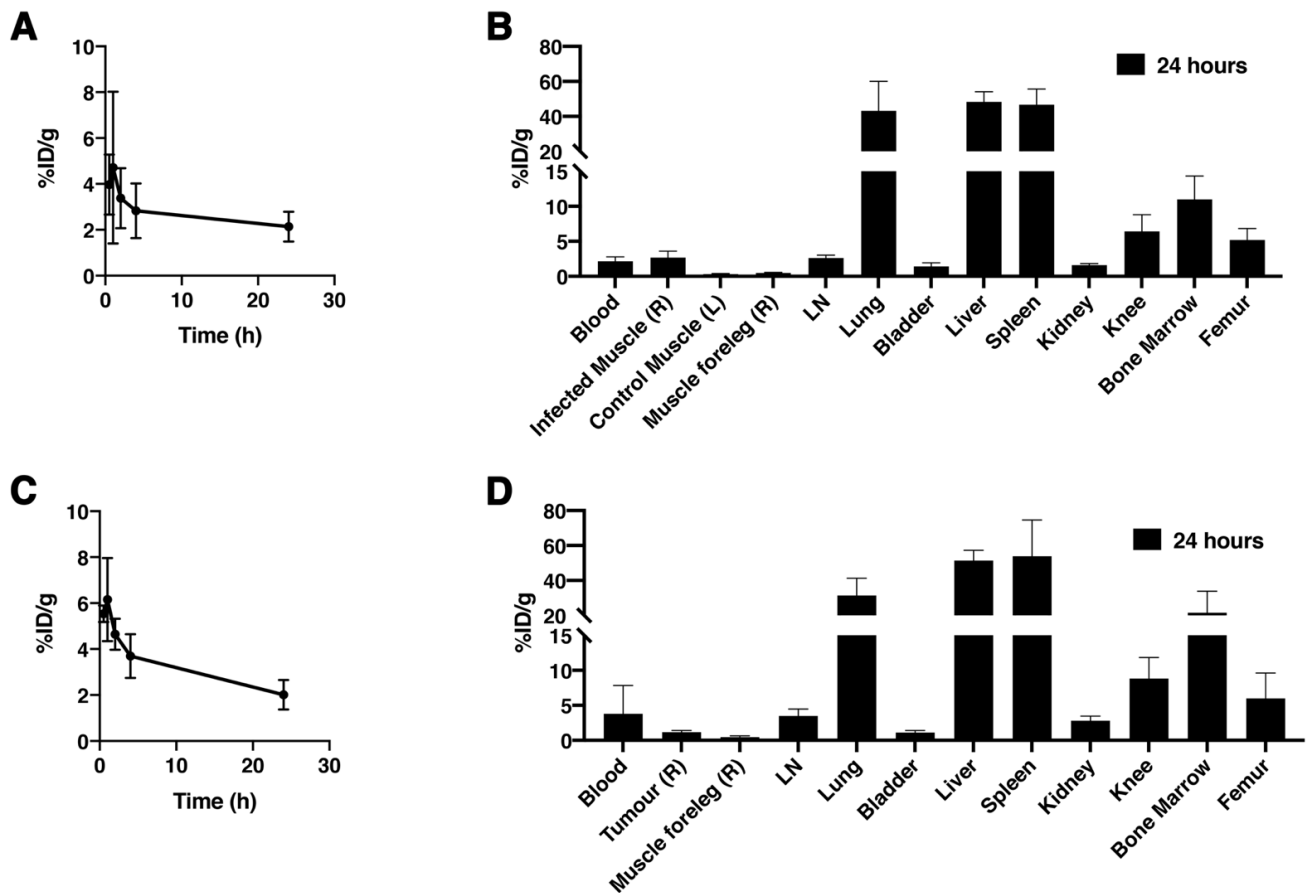


Figure 7. Biodistribution and blood clearance of $[^{89}\text{Zr}]\text{Zr}$ -THP-1 cells in *Staphylococcus aureus* (*S. aureus*) and MDA-MB-231 tumor models. Blood clearance and organs were measured after injection of the ex vivo labeled $[^{89}\text{Zr}]\text{Zr}$ -THP-1 cells in *S. aureus* (A,B) and MDA-MB-231 tumor (C,D) BALB/CAAn.Cg-Foxn1nu mice models. Blood was collected at 0.5, 1, 2, 4 and 24 h ($n = 3\text{--}5$). Organs were harvested after 24 h ($n = 4\text{--}5$). Additional information: infected muscle (R), *S. aureus* + blood (1:1) injected in right hind leg; control muscle, PBS + blood (1:1) injected in left hind leg; muscle foreleg (R), negative control muscle without any injection. Abbreviations: %ID/g, % injected dose per gram of organ; LN, lymph node.

In MDA-MB-231 tumor-bearing mice, $[^{89}\text{Zr}]\text{Zr}$ -THP-1 cells were also cleared from blood within 30 min. The spleen, liver, lung and bone marrow showed a high uptake of the radiolabeled cells at 24 h (Figure 7C,D and Table S3). The number of $[^{89}\text{Zr}]\text{Zr}$ -THP-1 cells accumulated at the tumor site was $0.11 \pm 0.05\%$ (corresponding to $5.55 \pm 2.53 \times 10^3$ cells) of the total injected cells, compared with $0.02 \pm 0.00\%$ ($0.96 \pm 0.19 \times 10^3$ cells) in the muscle of the foreleg. Moreover, a low PET signal in the tumor was detected at 4 h, which slightly increased at 24 h post-injection (Figure 8 and Videos S3 and S4).

Together, these sets of experiments show that it was feasible to track ex vivo $[^{89}\text{Zr}]\text{Zr}$ -PLGA-NH₂ NPs labeled THP-1 cells in two disease models.

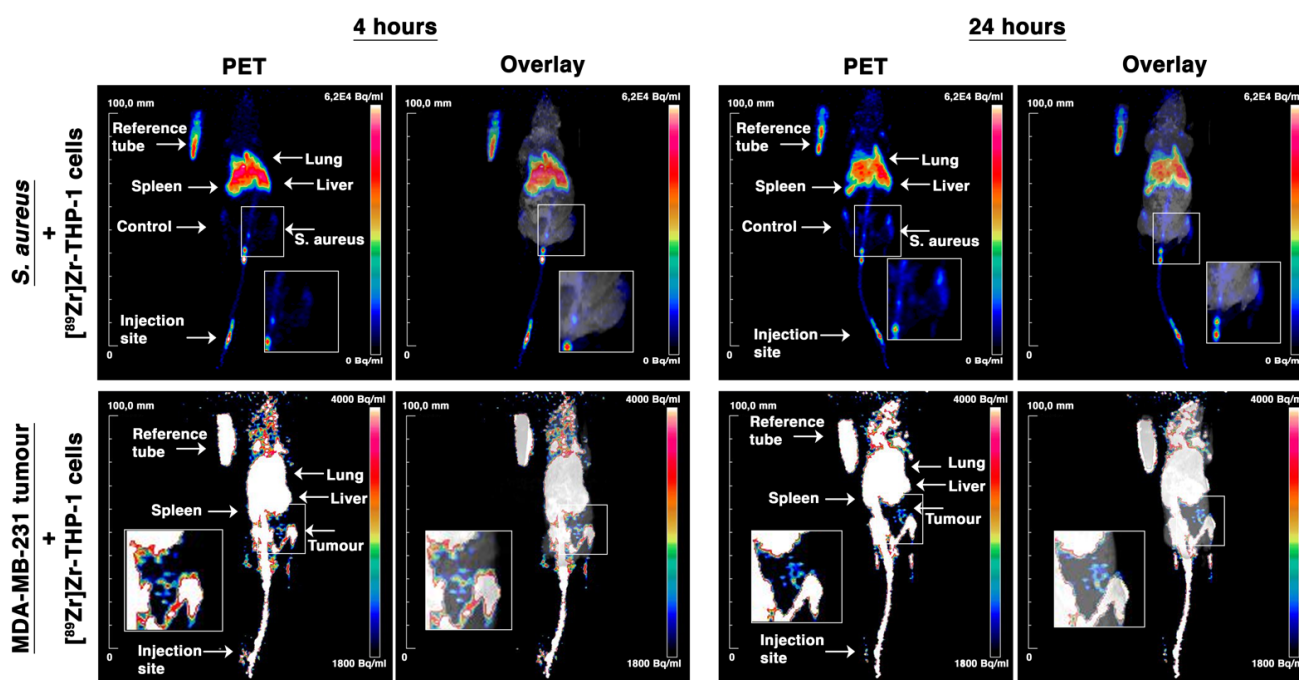


Figure 8. In vivo PET/MRI tracking of [^{89}Zr]Zr-THP-1 cells in *Staphylococcus aureus* (*S. aureus*) and MDA-MB-231 tumor models. *S. aureus* or MDA-MB-231 tumor cells were injected intramuscular or subcutaneously injected in BALB/CA N.N.Cg-Foxn1nu mice, respectively. Subsequently, ex vivo ^{89}Zr -labeled THP-1 cells ([^{89}Zr]Zr-THP-1, $5\text{--}5.8 \times 10^6$ cells/mouse) were injected intravenously and followed with PET/MRI for 24 h.

4. Discussion

PET is currently the most sensitive whole-body-imaging modality for clinical studies that is ideal for in vivo tracking of small numbers of labeled cells. The long-lived positron emitter $^{89}\text{Zr}^{4+}$ allows for imaging up to several days post-injection. This prompted us to explore the potential of [^{89}Zr]Zr-PLGA-NH $_2$ NPs for cell labeling and in vivo tracking with PET.

We previously developed PLGA-NH $_2$ -based NPs that were able to intrinsically complex and retain [^{111}In]InCl $_3$ for SPECT [31]. Here we demonstrated that these NPs also allow for intrinsic labeling with [^{89}Zr]ZrCl $_4$ for PET. As expected, labeling with non-radioactive Zr slightly increased the NPs' size and zeta potential.

PLGA-NH $_2$ NPs showed efficient labeling with [^{89}Zr]ZrCl $_4$, compared to normal PLGA NPs without -NH $_2$. In PBS and human serum, ^{89}Zr was retained for >80% by the NPs for up to 2 weeks. This indicates that the particles are able to retain the ^{89}Zr -label without the use of a chelator, such as desferrioxamine (DFO). However, when challenged with EDTA, ^{89}Zr was partly released from the particles, even at 0.1 mM (0.1 equivalents of EDTA) concentration. ^{89}Zr -release upon EDTA (1000 equivalents) challenge was also reported for DFO-conjugated trastuzumab, which showed a release of 25% and 50% in the first 24 h 7 days, respectively, which is slower than observed in our study [32]. From the literature, it was known that ^{89}Zr requires a strong Lewis base, such as OH $^-$ ions, and an 8-coordination for optimal binding and retention [33], which cannot be secured in the NPs, as chelation depends on free primary amine groups. However, for our application, the [^{89}Zr]Zr-PLGA-NH $_2$ NPs mainly serve the purpose of ex vivo cell labeling, and the release, in the first instance, is mainly limited to the intracellular compartments of the labeled cells. However, in the course of time or upon cell death, ^{89}Zr can be released and redistributed within the body.

The biodistribution of the [^{89}Zr]Zr-PLGA-NH $_2$ NPs was in line with our previous observations with [^{111}In]In-PLGA-NH $_2$ NPs [34]. The signal at the tail was probably due to partial s.c. injection of the NPs. Interestingly, the accumulation in liver was half that of [^{111}In]In-PLGA-NH $_2$ NPs [31]. Furthermore, in spleen, activity at day 14 was only

50 %ID/g for [^{89}Zr]Zr-PLGA-NH₂ NPs, while it was >100 %ID/g for [^{111}In]In-PLGA-NH₂ NPs. Accumulation of ^{89}Zr was observed in the femur and knee at day 3, but this did not increase further at day 14. From the literature, it is known that free ^{89}Zr released from the targeting vehicle has the tendency to accumulate in bone tissue [29]. The radioactivity in femur and knee might be explained by (I) the <5% free ^{89}Zr present during injection of the NPs, (II) ^{89}Zr -release from the NPs after injection or (III) macrophages and monocytes that take up the NPs and are present in or migrate to bone marrow.

The labeling of the THP-1 cells with [^{89}Zr]Zr-PLGA-NH₂ NPs was not very efficient, as only ~4% of the NPs was taken up by the cells. In general, cell labeling with [^{89}Zr]Zr-oxine is faster (15–30 min) and more efficient (10–40% labeling efficiency) when compared with NP-based cell labeling [35–38]. However, the specific activity of the NPs labeled cells was in range with the results from the literature, where human mesenchymal stem cells or chimeric antigen receptor (CAR) T cells were labeled for in vivo imaging with a broad range of specific activity of 0.009–0.370 MBq/10⁶ cells, using desferrioxamine or oxine as carrier [21,37,39,40]. Moreover, higher specific activity per cell is not desired, as this could lead to radiotoxicity [37]. Furthermore, ^{89}Zr was retained by the cells up to 48 h after incubation, which was comparable to [^{111}In]In-PLGA-NH₂-labeled moDC cells. Different type of cells (for example, CAR T cell and natural killer cells) labeled with [^{89}Zr]Zr-oxine showed a similar decrease of radioactivity over a period of 48 h [22,37,41]. The ^{89}Zr release from [^{89}Zr]Zr-oxine-labeled cells was also rapid for certain cell types (DCs and CAR T cells), i.e., >25% release after 2 days. These indicate that the NPs used in this study could play a role in cell labeling and in vivo tracking. However, future studies are needed to demonstrate feasibility of radiolabeling of other cell types, such as T cells. One strategy to enhance overall cellular uptake would be to modify the coating of NPs with, for example, cell-penetrating peptides or Lipofectamine [42–44]. Alternatively, to improve labeling of specific subsets of immune cells, NPs can be decorated with antibodies or peptides with the desired specificity [45,46].

In vivo studies showed that we were able to detect small numbers of labeled THP-1 cells, using PET. A clear signal was observed in mice which were transplanted s.c. with 10,000–100,000 [^{89}Zr]Zr-THP-1 cells (395–3950 Bq). Furthermore, minimal redistribution of radioactivity to other organs was observed, except for the femur and bone marrow, potentially caused by [^{89}Zr]Zr-THP-1 cells migrating to bone marrow or ^{89}Zr released from the cells. This indicates that ^{89}Zr is well retained inside cells.

Next, we injected [^{89}Zr]Zr-THP-1 cells i.v. and tracked their biodistribution in *S. aureus* inflammation model and a MDA-MB-231 tumor model. We detected a radioactive signal in the inflamed muscle and at the tumor site. However, it should be noted that the tumor accumulation was minimal, most likely because the tumor environment is less chemotactic compared with the *S. aureus* induced inflammation. Other studies have also developed techniques for PET-based cell tracking. For example, [^{89}Zr]Zr-oxine-based cell labeling has been evaluated in several studies with different type of cells and disease models. Recently, the potential of surface labeling with [^{89}Zr]Zr-DFO was shown by using human cardiopoietic stem cells for in vivo tracking in an ischemic-heart-failure mice model. Alternatively, a signal cell labeling and tracking was demonstrated with [^{68}Ga]Ga-mesoporous silica NPs, using PET [47]. The concept of single-cell tracking is highly challenging, as a high load of radioactivity per cell (>70 Bq) is required for accurate tracking. This could pose a problem in prolonged studies (24–72 h), since more radioactivity per cell would be required, as the half-life of ^{68}Ga is 67 min. Single-cell tracking would be interesting to study the behavior of that single cell; however, most effector mechanisms require cooperation with a multitude of other cells [48].

5. Conclusions

As PET is a highly sensitive imaging modality, in combination with novel cell-labeling approaches, it is ideally positioned for whole-body in vivo cell tracking. Here we expanded on our previous radiolabeling strategy and demonstrated for the first time that

[⁸⁹Zr]Zr-PLGA-NH₂ NPs can be used as a tool for cell labeling and sensitive in vivo cell tracking, using PET. For future (clinical) applications, however, cell-labeling efficiency can be improved by coating the surface of the NPs with cell-specific antibodies, peptides, nanobodies or other targeting agents.

Supplementary Materials: The following are available online at <https://www.mdpi.com/article/10.3390/cancers13205069/s1>. Figure S1: Over time particle stability in different buffers, Table S1: Biodistribution of [⁸⁹Zr]Zr-PLGA-NH₂ NPs at days 3 and 14 after intravenous tail injection in C57BL/6 mice, Data are expressed as % injected dose per gram (mean ± standard deviation, *n* = 3), Table S2: Biodistribution of [⁸⁹Zr]Zr-THP-1 cells at 24 h after subcutaneous injection, Data are expressed as % injected dose per gram (mean ± standard deviation, *n* = 4), Table S3: Biodistribution of [⁸⁹Zr]Zr-THP-1 cells at 24 h after intravenous injection in *Staphylococcus aureus* and MDA-MB-231 tumor models, Data are expressed as % injected dose per gram (mean ± standard deviation, *n* = 4–5), Video S1: *Staphylococcus aureus* 4 h, Video S2: *Staphylococcus aureus* 24 h, Video S3: MDA-MB-231 tumor 4 h, Video S4: MDA-MB-231 tumor 24 h.

Author Contributions: Conceptualization, M.K., M.S., E.H.J.G.A. and S.H.; methodology, M.K., M.S., E.H.J.G.A. and S.H.; software, M.K., K.R.G.C., M.B., A.K. and G.M.F., A.V., T.W.J.S., R.R. and N.K.v.R.; validation, M.K., K.R.G.C., M.B., A.K., G.M.F., A.V., T.W.J.S., R.R., N.K.v.R. and S.H.; formal analysis, M.K., K.R.G.C., M.B., A.K., G.M.F., A.V., T.W.J.S., R.R., N.K.v.R. and S.H.; investigation, M.K., K.R.G.C., M.B., A.K., G.M.F., A.V., T.W.J.S., R.R., N.K.v.R., M.S., E.H.J.G.A. and S.H.; resources, M.K., M.S., I.J.M.d.V., C.G.F., E.H.J.G.A. and S.H.; data curation, M.K., M.S., E.H.J.G.A. and S.H.; writing—original draft preparation, M.K., M.S., E.H.J.G.A. and S.H.; writing—review and editing, M.K., K.R.G.C., M.B., A.K., G.M.F., A.V., T.W.J.S., R.R., N.K.v.R., M.S., I.J.M.d.V., C.G.F., E.H.J.G.A. and S.H.; visualization, M.K., M.S., E.H.J.G.A. and S.H.; supervision, M.K., M.S., E.H.J.G.A. and S.H.; project administration, M.K., M.S., E.H.J.G.A. and S.H.; funding acquisition, M.S., I.J.M.d.V., C.G.F., E.H.J.G.A. and S.H. All authors have read and agreed to the published version of the manuscript.

Funding: EA received Junior Researcher grants from the Radboud Institute for Molecular Life Sciences (RIMLS) and Dutch Cancer Society Young Investigator Grant (project 12493) and is supported by a grant from the Radboud Oncologie Fonds/Stichting Bergh in het Zadel, partner of Dutch Cancer Society (KUN2015-8106). This study received funding from the Innovative Medicines Initiative 2 Joint Undertaking under grant agreement No 116106. This Joint Undertaking received support from the European Union's Horizon 2020 research and innovation program and EFPIA. SH is supported by the Netherlands Organisation for Scientific Research (NWO, project number 91617039), and the Dutch Cancer Society (KWF, project number 10099). MS received a European Research Council (ERC) starting grant (CoNQUeST, grant 336454) and Proof of Concept (CoNQUeST, grant 713524), grant 14716 from The Netherlands organisation for scientific research NWO-TTW and a grant from European Research Area Network on Cardiovascular Disease (ERA-CVD, SCAN, 2017T097).

Institutional Review Board Statement: Experiments were performed in accordance with the guidelines set for animal care of the Nijmegen and European Animal Experiments Committee (CCD application 2018-0011 and 2020-0007).

Informed Consent Statement: Not applicable.

Data Availability Statement: The data presented in this study are available in this article and supplementary material. The raw data are available upon request.

Acknowledgments: We would also like to thank Olga Koshkina, Edyta Swider and Alexander H.J. Staal from the Tumor Immunology department of the Radboud University Medical Center for their helpful discussions. We would also like to thank Peter Laverman and Mark Rijpkema from the Medical Imaging department of the Radboud University Medical Center for their helpful discussions. We would also like to thank Raffaella Rossin and Thuur van Onzen from Tagworks Pharmaceuticals for their helpful discussions.

Conflicts of Interest: The authors declare the following competing financial interest(s): M.S. and N.K.v.R. work for Cenya Imaging BV, The Netherlands.

References

1. Harari, A.; Graciotti, M.; Bassani-Sternberg, M.; Kandalaf, L.E. Antitumour Dendritic Cell Vaccination in a Priming and Boosting Approach. *Nat. Rev. Drug Discov.* **2020**, *19*, 635–652. [[CrossRef](#)] [[PubMed](#)]
2. Boudewijns, S.; Bloemendal, M.; de Haas, N.; Westdorp, H.; Bol, K.F.; Schreibeit, G.; Aarntzen, E.H.J.G.; Lesterhuis, W.J.; Gorris, M.A.J.; Croockewit, A.; et al. Autologous Monocyte-Derived DC Vaccination Combined with Cisplatin in Stage III and IV Melanoma Patients: A Prospective, Randomized Phase 2 Trial. *Cancer Immunol. Immunother.* **2020**, *69*, 477–488. [[CrossRef](#)]
3. D'Agostino, M.; Raje, N. Anti-BCMA CAR T-Cell Therapy in Multiple Myeloma: Can We Do Better? *Leukemia* **2020**, *34*, 21–34. [[CrossRef](#)] [[PubMed](#)]
4. Singh, A.K.; McGuirk, J.P. CAR T Cells: Continuation in a Revolution of Immunotherapy. *Lancet Oncol.* **2020**, *21*, e168–e178. [[CrossRef](#)]
5. Lee, S.; Ko, Y.; Kim, T.J. Homeostasis and Regulation of Autoreactive B Cells. *Cell. Mol. Immunol.* **2020**, *17*, 561–569. [[CrossRef](#)] [[PubMed](#)]
6. Volkov, M.; Schie, K.A.; Woude, D. Autoantibodies and B Cells: The ABC of Rheumatoid Arthritis Pathophysiology. *Immunol. Rev.* **2020**, *294*, 148–163. [[CrossRef](#)]
7. Schwartz, D.M.; Burma, A.M.; Kitakule, M.M.; Luo, Y.; Mehta, N.N. T Cells in Autoimmunity-Associated Cardiovascular Diseases. *Front. Immunol.* **2020**, *11*, 588776. [[CrossRef](#)]
8. Paijens, S.T.; Vledder, A.; de Bruyn, M.; Nijman, H.W. Tumor-Infiltrating Lymphocytes in the Immunotherapy Era. *Cell. Mol. Immunol.* **2021**, *18*, 842–859. [[CrossRef](#)] [[PubMed](#)]
9. Lin, B.; Du, L.; Li, H.; Zhu, X.; Cui, L.; Li, X. Tumor-Infiltrating Lymphocytes: Warriors Fight against Tumors Powerfully. *Biomed. Pharmacother.* **2020**, *132*, 110873. [[CrossRef](#)]
10. Kircher, M.F.; Allport, J.R.; Graves, E.E.; Love, V.; Josephson, L.; Lichtman, A.H.; Weissleder, R. In Vivo High Resolution Three-Dimensional Imaging of Antigen-Specific Cytotoxic T-Lymphocyte Trafficking to Tumors. *Cancer Res.* **2003**, *63*, 6838–6846.
11. Zhou, X.Y.; Tay, Z.W.; Chandrasekharan, P.; Yu, E.Y.; Hensley, D.W.; Orendorff, R.; Jeffris, K.E.; Mai, D.; Zheng, B.; Goodwill, P.W.; et al. Magnetic Particle Imaging for Radiation-Free, Sensitive and High-Contrast Vascular Imaging and Cell Tracking. *Curr. Opin. Chem. Biol.* **2018**, *45*, 131–138. [[CrossRef](#)] [[PubMed](#)]
12. Panagiotopoulos, N.; Vogt, F.; Barkhausen, J.; Buzug, T.M.; Duschka, R.L.; Lütke-Buzug, K.; Ahlberg, M.; Bringout, G.; Debbeler, C.; Gräser, M.; et al. Magnetic Particle Imaging: Current Developments and Future Directions. *Int. J. Nanomed.* **2015**, *10*, 3097. [[CrossRef](#)]
13. Graeser, M.; Thieben, F.; Szwargulski, P.; Werner, F.; Gdaniec, N.; Boberg, M.; Griese, F.; Möddel, M.; Ludewig, P.; van de Ven, D.; et al. Human-Sized Magnetic Particle Imaging for Brain Applications. *Nat. Commun.* **2019**, *10*, 1936. [[CrossRef](#)] [[PubMed](#)]
14. Mason, E.E.; Cooley, C.Z.; Cauley, S.F.; Griswold, M.A.; Conolly, S.M.; Wald, L.L. Design Analysis of an MPI Human Functional Brain Scanner. *Int. J. Magn. Part. Imaging* **2017**, *3*, 12. [[CrossRef](#)]
15. Thakur, M.L.; Segal, A.W.; Louis, L.; Welch, M.J.; Hopkins, J.; Peters, T.J. Indium-111-Labeled Cellular Blood Components: Mechanism of Labeling and Intracellular Location in Human Neutrophils. *J. Nucl. Med. Off. Publ. Soc. Nucl. Med.* **1977**, *18*, 1022–1026.
16. Roca, M.; de Vries, E.F.J.; Jamar, F.; Israel, O.; Signore, A. Guidelines for the Labelling of Leucocytes with ¹¹¹In-Oxine. *Eur. J. Nucl. Med. Mol. Imaging* **2010**, *37*, 835–841. [[CrossRef](#)]
17. De Vries, E.F.J.; Roca, M.; Jamar, F.; Israel, O.; Signore, A. Guidelines for the Labelling of Leucocytes with ^{99m}Tc-HMPAO. *Eur. J. Nucl. Med. Mol. Imaging* **2010**, *37*, 842–848. [[CrossRef](#)]
18. Bin Othman, M.F.; Mitry, N.R.; Lewington, V.J.; Blower, P.J.; Terry, S.Y.A. Re-Assessing Gallium-67 as a Therapeutic Radionuclide. *Nucl. Med. Biol.* **2017**, *46*, 12–18. [[CrossRef](#)]
19. Kassis, A.I.; Adelstein, S.J. Chemotoxicity of Indium-111 Oxine in Mammalian Cells. *J. Nucl. Med. Off. Publ. Soc. Nucl. Med.* **1985**, *26*, 187–190.
20. Cherry, S.R.; Jones, T.; Karp, J.S.; Qi, J.; Moses, W.W.; Badawi, R.D. Total-Body PET: Maximizing Sensitivity to Create New Opportunities for Clinical Research and Patient Care. *J. Nucl. Med.* **2018**, *59*, 3–12. [[CrossRef](#)]
21. Asiedu, K.O.; Ferdousi, M.; Ton, P.T.; Adler, S.S.; Choyke, P.L.; Sato, N. Bone Marrow Cell Homing to Sites of Acute Tibial Fracture: ⁸⁹Zr-Oxine Cell Labeling with Positron Emission Tomographic Imaging in a Mouse Model. *EJNMMI Res.* **2018**, *8*, 109. [[CrossRef](#)]
22. Patrick, P.S.; Kolluri, K.K.; Zaw Thin, M.; Edwards, A.; Sage, E.K.; Sanderson, T.; Weil, B.D.; Dickson, J.C.; Lythgoe, M.F.; Lowdell, M.; et al. Lung Delivery of MSCs Expressing Anti-Cancer Protein TRAIL Visualised with ⁸⁹Zr-Oxine PET-CT. *Stem Cell Res. Ther.* **2020**, *11*, 256. [[CrossRef](#)]
23. Charoenphun, P.; Meszaros, L.K.; Chuamsaamarkkee, K.; Sharif-Paghaleh, E.; Ballinger, J.R.; Ferris, T.J.; Went, M.J.; Mullen, G.E.D.; Blower, P.J. [⁸⁹Zr]Oxinate4 for Long-Term in Vivo Cell Tracking by Positron Emission Tomography. *Eur. J. Nucl. Med. Mol. Imaging* **2015**, *42*, 278–287. [[CrossRef](#)]
24. Davidson-Moncada, J.; Sato, N.; Hoyt, R.F.; Reger, R.N.; Thomas, M.; Clevenger, R.; Metzger, M.E.; Donahue, R.E.; Eclarinal, P.C.; Szajek, L.; et al. A Novel Method to Study the in Vivo Trafficking and Homing of Adoptively Transferred NK Cells in Rhesus Macaques and Humans. *Blood* **2014**, *124*, 659. [[CrossRef](#)]
25. Keliher, E.J.; Yoo, J.; Nahrendorf, M.; Lewis, J.S.; Marinelli, B.; Newton, A.; Pittet, M.J.; Weissleder, R. ⁸⁹Zr-Labeled Dextran Nanoparticles Allow in Vivo Macrophage Imaging. *Bioconjug. Chem.* **2011**, *22*, 2383–2389. [[CrossRef](#)]

26. Patrick, P.S.; Bogart, L.K.; Macdonald, T.J.; Southern, P.; Powell, M.J.; Zaw-Thin, M.; Voelcker, N.H.; Parkin, I.P.; Pankhurst, Q.A.; Lythgoe, M.F.; et al. Surface Radio-Mineralisation Mediates Chelate-Free Radiolabelling of Iron Oxide Nanoparticles. *Chem. Sci.* **2019**, *10*, 2592–2597. [[CrossRef](#)]
27. Pérez-Medina, C.; Tang, J.; Abdel-Atti, D.; Hogstad, B.; Merad, M.; Fisher, E.A.; Fayad, Z.A.; Lewis, J.S.; Mulder, W.J.M.; Reiner, T. PET Imaging of Tumor-Associated Macrophages with ⁸⁹Zr-Labeled High-Density Lipoprotein Nanoparticles. *J. Nucl. Med.* **2015**, *56*, 1272–1277. [[CrossRef](#)] [[PubMed](#)]
28. Fairclough, M.; Ellis, B.; Boutin, H.; Jones, A.K.P.; McMahon, A.; Alzabin, S.; Gennari, A.; Prenant, C. Development of a Method for the Preparation of Zirconium-89 Radiolabelled Chitosan Nanoparticles as an Application for Leukocyte Trafficking with Positron Emission Tomography. *Appl. Radiat. Isot.* **2017**, *130*, 7–12. [[CrossRef](#)] [[PubMed](#)]
29. Abou, D.S.; Ku, T.; Smith-Jones, P.M. In Vivo Biodistribution and Accumulation of ⁸⁹Zr in Mice. *Nucl. Med. Biol.* **2011**, *38*, 675–681. [[CrossRef](#)] [[PubMed](#)]
30. Perrin, J.; Capitaio, M.; Mougín-Degraef, M.; Guérard, F.; Faivre-Chauvet, A.; Rbah-Vidal, L.; Gaschet, J.; Guilloux, Y.; Kraeber-Bodéré, F.; Chérel, M.; et al. Cell Tracking in Cancer Immunotherapy. *Front. Med.* **2020**, *7*, 34. [[CrossRef](#)] [[PubMed](#)]
31. Krekorian, M.; Sandker, G.G.W.; Cortenbach, K.R.G.; Tagit, O.; van Riessen, N.K.; Raavé, R.; Srinivas, M.; Figdor, C.G.; Heskamp, S.; Aarntzen, E.H.J.G. Characterization of Intrinsically Radiolabeled Poly(Lactic-Co -Glycolic Acid) Nanoparticles for Ex Vivo Autologous Cell Labeling and in Vivo Tracking. *Bioconjug. Chem.* **2021**, *32*, 1802–1811. [[CrossRef](#)]
32. Raavé, R.; Sandker, G.; Adumeau, P.; Jacobsen, C.B.; Mangin, F.; Meyer, M.; Moreau, M.; Bernhardt, C.; Da Costa, L.; Dubois, A.; et al. Direct Comparison of the in Vitro and in Vivo Stability of DFO, DFO* and DFOcyclo* for ⁸⁹Zr-ImmunoPET. *Eur. J. Nucl. Med. Mol. Imaging* **2019**, *46*, 1966–1977. [[CrossRef](#)]
33. Holland, J.P.; Divilov, V.; Bander, N.H.; Smith-Jones, P.M.; Larson, S.M.; Lewis, J.S. ⁸⁹Zr-DFO-J591 for ImmunoPET of Prostate-Specific Membrane Antigen Expression In Vivo. *J. Nucl. Med.* **2010**, *51*, 1293–1300. [[CrossRef](#)]
34. Staal, A.H.J.; Becker, K.; Tagit, O.; Koen van Riessen, N.; Koshkina, O.; Veltien, A.; Bouvain, P.; Cortenbach, K.R.G.; Scheenen, T.; Flögel, U.; et al. In Vivo Clearance of ¹⁹F MRI Imaging Nanocarriers Is Strongly Influenced by Nanoparticle Ultrastructure. *Biomaterials* **2020**, *261*, 120307. [[CrossRef](#)] [[PubMed](#)]
35. Sato, N.; Wu, H.; Asiedu, K.O.; Szajek, L.P.; Griffiths, G.L.; Choyke, P.L. ⁸⁹Zr-Oxine Complex PET Cell Imaging in Monitoring Cell-Based Therapies. *Radiology* **2015**, *275*, 490–500. [[CrossRef](#)]
36. Man, F.; Khan, A.A.; Carrascal-Miniño, A.; Blower, P.J.; de Rosales, R.T. A Kit Formulation for the Preparation of [⁸⁹Zr]Zr(Oxinate)₄ for PET Cell Tracking: White Blood Cell Labelling and Comparison with [¹¹¹In]In(Oxinate). *Nucl. Med. Biol.* **2020**, *90*, 31–40. [[CrossRef](#)]
37. Weist, M.R.; Starr, R.; Aguilar, B.; Chea, J.; Miles, J.K.; Poku, E.; Gerdts, E.; Yang, X.; Priceman, S.J.; Forman, S.J.; et al. PET of Adoptively Transferred Chimeric Antigen Receptor T Cells with ⁸⁹Zr-Oxine. *J. Nucl. Med.* **2018**, *59*, 1531–1537. [[CrossRef](#)]
38. Liu, Y.; Zhao, X.; Ding, J.; Xing, Y.; Zhou, M.; Wang, X.; Zhu, W.; Huo, L.; Yang, J. Evidence of Accumulated Endothelial Progenitor Cells in the Lungs of Rats with Pulmonary Arterial Hypertension by ⁸⁹Zr-Oxine PET Imaging. *Mol. Ther. Methods Clin. Dev.* **2020**, *17*, 1108–1117. [[CrossRef](#)]
39. Bansal, A.; Pandey, M.K.; Demirhan, Y.E.; Nesbitt, J.J.; Crespo-Diaz, R.J.; Terzic, A.; Behfar, A.; DeGrado, T.R. Novel ⁸⁹Zr Cell Labeling Approach for PET-Based Cell Trafficking Studies. *EJNMMI Res.* **2015**, *5*, 19. [[CrossRef](#)]
40. Bansal, A.; Pandey, M.K.; Yamada, S.; Goyal, R.; Schmit, N.R.; Jeon, R.; Nesbitt, J.J.; Witt, T.A.; Singh, R.D.; Gunderson, T.M.; et al. [⁸⁹Zr]Zr-DBN Labeled Cardiopoietic Stem Cells Proficient for Heart Failure. *Nucl. Med. Biol.* **2020**, *90*, 23–30. [[CrossRef](#)]
41. Sato, N.; Stringaris, K.; Davidson-Moncada, J.K.; Reger, R.; Adler, S.S.; Dunbar, C.; Choyke, P.L.; Childs, R.W. In Vivo Tracking of Adoptively Transferred Natural Killer Cells in Rhesus Macaques Using ⁸⁹Zirconium-Oxine Cell Labeling and PET Imaging. *Clin. Cancer Res.* **2020**, *26*, 2573–2581. [[CrossRef](#)] [[PubMed](#)]
42. Van Bracht, E.; Versteegden, L.R.M.; Stolle, S.; Verdurmen, W.P.R.; Woestenenk, R.; Raavé, R.; Hafmans, T.; Oosterwijk, E.; Brock, R.; van Kuppevelt, T.H.; et al. Enhanced Cellular Uptake of Albumin-Based Lyophilosomes When Functionalized with Cell-Penetrating Peptide TAT in HeLa Cells. *PLoS ONE* **2014**, *9*, e110813. [[CrossRef](#)] [[PubMed](#)]
43. Cardarelli, F.; Digiacomo, L.; Marchini, C.; Amici, A.; Salomone, F.; Fiume, G.; Rossetta, A.; Gratton, E.; Pozzi, D.; Caracciolo, G. The Intracellular Trafficking Mechanism of Lipofectamine-Based Transfection Reagents and Its Implication for Gene Delivery. *Sci. Rep.* **2016**, *6*, 25879. [[CrossRef](#)]
44. Silva, S.; Almeida, A.; Vale, N. Combination of Cell-Penetrating Peptides with Nanoparticles for Therapeutic Application: A Review. *Biomolecules* **2019**, *9*, 22. [[CrossRef](#)] [[PubMed](#)]
45. Kim, K.-T.; Lee, J.-Y.; Kim, D.-D.; Yoon, I.-S.; Cho, H.-J. Recent Progress in the Development of Poly(Lactic-Co-Glycolic Acid)-Based Nanostructures for Cancer Imaging and Therapy. *Pharmaceutics* **2019**, *11*, 280. [[CrossRef](#)] [[PubMed](#)]
46. Juan, A.; Cimas, F.J.; Bravo, I.; Pandiella, A.; Ocaña, A.; Alonso-Moreno, C. An Overview of Antibody Conjugated Polymeric Nanoparticles for Breast Cancer Therapy. *Pharmaceutics* **2020**, *12*, 802. [[CrossRef](#)]
47. Jung, K.O.; Kim, T.J.; Yu, J.H.; Rhee, S.; Zhao, W.; Ha, B.; Red-Horse, K.; Gambhir, S.S.; Pratz, G. Whole-Body Tracking of Single Cells via Positron Emission Tomography. *Nat. Biomed. Eng.* **2020**, *4*, 835–844. [[CrossRef](#)]
48. Weigel, B.; den Boer, A.T.; Wagena, E.; Broen, K.; Dolstra, H.; de Boer, R.J.; Figdor, C.G.; Textor, J.; Friedl, P. Cancer Cell Elimination by Cytotoxic T Cell Cooperation and Additive Damage. *Immunology* **2020**. [[CrossRef](#)]